

# Controlled Noncontact Manipulation of Nonmagnetic Untethered Microbeads Orbiting Two-Tailed Soft Microrobot

Islam S. M. Khalil , *Member, IEEE*, Anke Klingner , Youssef Hamed , Yehia S. Hassan ,  
and Sarthak Misra , *Member, IEEE*

**Abstract**—A rotating two-tailed soft microrobot induces a frequency dependent flow-field in low Reynolds number fluids. We use this flow-field to achieve noncontact manipulation of nonmagnetic microbeads with average diameter of  $30\ \mu\text{m}$  in 2-D space. Our noncontact manipulation strategy capitalizes on exerting a rotational magnetic torque on the magnetic dipole of the microrobot. The induced flow-field enables microbeads in the surrounding fluid to orbit the microrobot along a sprocketlike trajectory due to a periodic and asymmetric flow-field caused by the two tails. A hydrodynamic model of the two-tailed microrobot and the orbiting microbeads is developed based on the method of regularized Stokeslets for computing Stokes flows. The relations between the angular velocity of the orbiting microbeads and the rotation frequency of the microrobot, their proximity ( $p$ ), and tail length ratio of the microrobots are studied theoretically and experimentally. Our simulations and experimental results show that the angular velocity of the orbiting microbeads decreases nearly as  $|p|^{-2}$  with the distance to the microrobot and its tail length ratio. We also demonstrate closed-loop control of the microbeads toward target positions along sprocketlike trajectories with an average position error of  $23.1 \pm 9.1\ \mu\text{m}$  ( $n = 10$ ), and show the ability to swim away without affecting the positioning accuracy after manipulation.

**Index Terms**—Control, flow-field, low Reynolds numbers, magnetic, manipulation, noncontact, orbiting, soft microrobots, two-tailed.

## I. INTRODUCTION

ONE of the motivations for the development of microrobots is the continuous demand to sort, manipulate, and assemble micro-objects at microscale with high level of accuracy. Microrobots can function as microgrippers or micromanipulators to move micro-objects with or without direct contact [1]–[3]. A major challenge that hinders this development is the complexity to achieve successful releases at the desired position. At this scale, surface and drag forces have a significant influence on the interactions between the microrobot and the micro-object. The adhesive forces between a microgripper (or any manipulation tool) and an object result in stickiness, and thus prevent its release at the desired position. In the case of contact-free manipulation, the fluidic trapping between the microrobot and the micro-object also influences the positioning accuracy after manipulation. Therefore, several microrobot designs [2], [4], actuation techniques [5], [6], and manipulation strategies [7]–[9] have been proposed to meet this need and overcome these challenges.

In contrast to manipulator-based micromanipulation [10]–[12], untethered microgrippers and microrobots are capable of navigation in a low Reynolds number ( $Re$ ) regime and can be remotely triggered by chemical [13], thermal [14], [15], and magnetic stimuli [4], [16]. Randhawa *et al.* [13] have demonstrated pick and place of tubes and beads using chemo-mechanically triggered microgrippers, consisting of a trilayer hinge joint. This microgripper has the ability to be opened and closed by residual stresses, but its dependence on chemicals puts limits on the material of micro-objects and is not suitable under biological conditions. This biocompatibility limitation has been overcome through biochemically and thermally triggered microgrippers [14]. Fusco *et al.* [15] have demonstrated magnetic-based remote actuation and photothermal actuation of light responsive self-folding microrobot. Diller and Sitti [4] have used uniform magnetic field and field gradient to achieve programmable 3-D microassembly using untethered magnetic microgrippers, and demonstrated parallel operation by multiple microgrippers. Zhang *et al.* [17] have also demonstrated autonomous 3-D microgripping and cargo delivery with

Manuscript received January 17, 2020; accepted April 2, 2020. This work was supported in part by the Science and Technology Development Fund in Egypt under Grant 23016 and in part by the European Research Council under the European Union’s Horizon 2020 Research and Innovation programme under Grant 638428 project ROBOTAR: Robot-Assisted Flexible Needle Steering for Targeted Delivery of Magnetic Agents. This paper was recommended for publication by Associate Editor R. Hatton and Editor P. Dupont upon evaluation of the reviewers’ comments. (Corresponding author: Islam S. M. Khalil.)

Islam S. M. Khalil is with the Department of Biomechanical Engineering, Faculty of Engineering Technology, University of Twente, 7500 AE Enschede, The Netherlands (e-mail: i.s.m.khalil@utwente.nl).

Anke Klingner is with the Department of Physics, The German University in Cairo, New Cairo City 11835, Egypt (e-mail: anke.klingner@guc.edu.eg).

Youssef Hamed and Yehia S. Hassan are with the Department of Mechatronics Engineering, Faculty of Engineering and Material Science, The German University in Cairo, New Cairo City 11835, Egypt (e-mail: youssef.sabry@student.guc.edu.eg; yehia.ibrahim@student.guc.edu.eg).

Sarthak Misra is with the Department of Biomechanical Engineering, Faculty of Engineering Technology, University of Twente, 7500 AE Enschede, The Netherlands, and also with the Department of Biomedical Engineering, University of Groningen and University Medical Center Groningen, 9713 AV Groningen, The Netherlands (e-mail: s.misra@utwente.nl).

This article has supplementary downloadable multimedia material available at <https://ieeexplore.ieee.org> provided by the authors. This includes a video file, which demonstrates closed-loop noncontact manipulation of microbeads using two-tailed soft microrobots. This material is 32.8 MB in size.

Color versions of one or more of the figures in this article are available online at <https://ieeexplore.ieee.org>.

Digital Object Identifier 10.1109/TRO.2020.2990768

maximum magnetic field gradient of 0.31 T/m in a workspace of a 2-cm cube.

An alternative micromanipulation approach is to achieve fluidic trapping of micro-objects using microrobots or utilize fluid boundary layers to produce contact-free motion [1], [2]. Pawashe *et al.* [18] have utilized stick-slip motion of a magnetically actuated microrobot (maximum magnetic field of 3 mT) on a surface to create local fluid flow and push (front and side pushing) microspheres without contact within a workspace of  $4.6 \times 3.4 \text{ mm}^2$ . It has also been shown that microassembly using noncontact side pushing is more effective than front pushing. Ye *et al.* [19] have also presented a noncontact manipulation method using locally induced rotational fluid flows. These flows are created by groups of untethered magnetic micromanipulators that are trapped at prescribed positions near a boundary to create a virtual fluidic channel using field strength of 5 mT in a workspace of  $30 \times 30 \times 1 \text{ mm}^3$ . Tung *et al.* [20] have also used the fluidic trapping method for the manipulation of micro-objects in liquid using a transversely magnetized rolling robot, at magnetic field of 5 mT. The manipulation is achieved by the transmitted force to the manipulated objects through the flow-field of the medium in which the object is immersed. With these noncontact manipulation strategies, even more so than with other contact manipulation techniques, we can mitigate the contamination of biological samples caused by direct contact during grasping, and hence noncontact manipulation is attractive in handling and sorting biological organisms. It is also important to create fluidic trapping of micro-objects away from a surface and without magnetic field gradients. Peyer *et al.* [2] have shown the capability of artificial bacterial flagella to create rotational fluid flow and manipulate microbeads. In this case, the microrobot is moved using rotating magnetic fields to a prescribed position, tuned to reach stationary position with zero translational velocity, and create local flow-fields and maintain its location during manipulation.

In this work, fluidic trapping of micro-objects is combined with flagellar swimming of a soft microrobot to achieve noncontact micromanipulation. This combination is important for nonneutrally buoyant microrobots to achieve noncontact manipulation without stick-slip motion or rolling on a nearby surface. In addition, implementing noncontact micromanipulation using soft microrobots maintain their desirable properties (simple in design and manufacturing, less density, higher level of biodegradability) compared to rigid microrobots [21]. We use soft two-tailed microrobots to achieve closed-loop noncontact manipulation of microbeads in 2-D space. The microrobots achieve flagellar propulsion using oscillating magnetic fields and noncontact manipulation of the microbeads using rotating magnetic fields (see Fig. 1) in milliTesla range without dependence on the magnetic field gradient, thereby extending the range of the current noncontact manipulation techniques [1], [3], [17], [19]. We model and characterize the flow-field created by one- and two-tailed rigid and flexible microrobots based on the method of regularized Stokeslets [22]. This flow-field allows microbeads to orbit the rotating microrobot without contact under the influence of rotating magnetic fields in milliTesla range. The two tails enable the microrobot to swim back and forth toward the microbead (and away from the microbead after

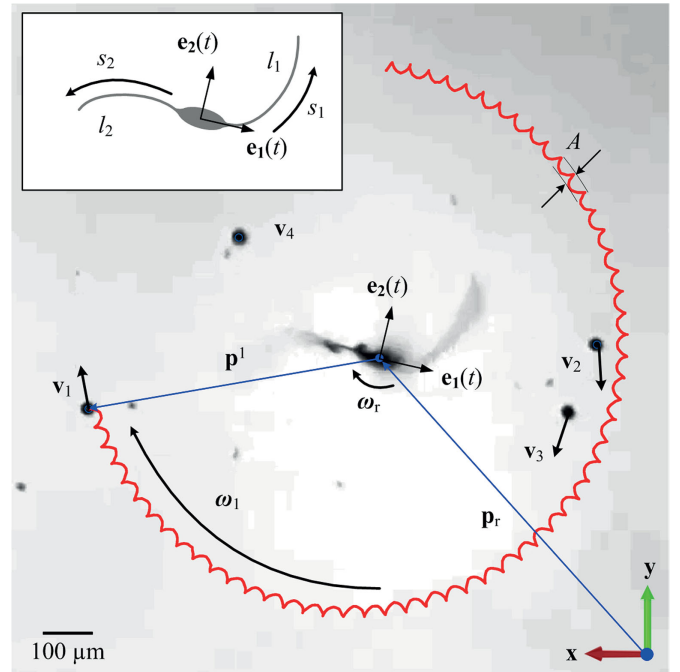


Fig. 1. Nonmagnetic microbeads orbit rotating two-tailed microrobot under the influence of its flow-field. The  $i$ th microbead moves at a linear velocity of  $\mathbf{v}_i$  and  $\mathbf{p}_i$  ( $i = 1, \dots, 4$ ) is its position vector from the two-tailed microrobot.  $\mathbf{e}_1(t)$  and  $\mathbf{e}_2(t)$  are orthonormal vectors of the material frame of the two-tailed microrobot. The sprocketlike trajectory (with amplitude  $A$ ) of the microbeads is generated by the asymmetric flow-field of the two tails of the microrobot. The tails have length of  $l_1$  and  $l_2$  and their shape is characterized by the deformation as a function of the arc length  $s_1$  and  $s_2$ . Rotation of the two-tailed microrobot at angular velocity  $\omega_r$  results in rotation of the  $i$ th microbeads at angular velocity of  $\omega_i$ .

manipulation) and rotate to achieve closed-loop manipulation without contact.

The remainder of this article is organized as follows. In Section II, we discuss the physics of the interactions between the two-tailed microrobot and the immersed objects in the medium, with descriptions of the control and manipulation problems. Section III provides the experimental characterization of the orbiting microbeads and provides analysis on the relation between the tail length ratio of the two-tailed microrobot and the angular velocity of the orbiting microbeads. Section IV presents our closed-loop control strategy and experimental results. Finally, Section V concludes this article and provides directions for future work.

## II. MODELING OF NONMAGNETIC MICROBEADS ORBITING A ROTATING TWO-TAILED MICROROBOT

In an inertialess viscous medium, characterized by low- $Re$ , the resulting flow-field of an externally actuated microrobot influences the surrounding objects. We consider the dynamics of a two-tailed microrobot owing to its ability to achieve flagellar propulsion and create relatively high flow-fields via its rotating tails. Flow-fields can also be created by a spherical or a prolate spheroidal magnets. However, these magnets have to be pulled (or depend on a surface to roll [20] or move using stick-slip motion [1], [18] using magnetic fields) with a magnetic force and their workspace is limited by the projection distance of the field gradient [23]. In addition, flow-fields can be also created

by a rotating one-tailed microrobot. However, the additional tail increases the angular velocity of the orbiting microbeads and enables the microrobot to swim back and forth to enhance the manipulation accuracy.

### A. Governing Dynamics

The soft two-tailed microrobot consists of a prolate spheroidal head of length  $2a$  and radius  $b$ . The head is rigidly attached to two ultrathin flexible tails of bending stiffness  $\kappa$ , diameter  $2r_t$ , and lengths of  $l_1$  and  $l_2$ . The two-tailed microrobots are fabricated by electrospinning a solution of polystyrene in dimethylformamide and magnetic particles. These particles are embedded into the head and provide an average magnetic moment  $\mathbf{M}$ . Under the influence of an external magnetic field  $\mathbf{B}$ , the dipole moment of the two-tailed microrobot enables directional control along the field lines. The following two magnetic field patterns are applied:

- 1) uniform fields with sinusoidally varying orthogonal components to achieve flagellar swim (with small tail deformation) and travel to (or away from) the manipulation site;
- 2) rotating magnetic fields to couple the microbeads to a rotating microrobot (with large tail deformation) and allow them to orbit without contact (see Fig. 1).

The two-tailed microrobot is allowed to swim in a medium with viscosity  $\eta$ , characterized by low- $Re$  hydrodynamics ( $Re = \rho v_x(l_1 + l_2 + 2a)/\eta$ ) on the order of  $\mathcal{O}(10^{-5})$ , where  $\rho$  and  $\eta$  are the density and viscosity of the medium, respectively, and  $v_x$  is the forward swimming speed of the microrobot. This medium contains nonmagnetic spherical microbeads with an average diameter  $2R_p$ . The governing fluid mechanics equations for the two-tailed microrobot and the orbiting microbeads at low- $Re$  are given by the following Stokes equation:

$$\eta \nabla^2 \mathbf{u} + \mathbf{f} - \nabla p = 0 \quad (1)$$

$$\nabla \cdot \mathbf{u} = 0 \quad (2)$$

where  $\mathbf{u}$  is the velocity vector field. Further,  $\mathbf{f}$  and  $p$  are the body force of the two-tailed microrobot acting on the fluid and the scalar pressure field, respectively. The velocity field, due to a force at a point, can be approximated based on the method of regularized Stokeslets. Therefore, we calculate the forces imparted to the fluid by the two-tailed microrobot using the force balance between the propulsive forces of the tails and the drag force on the head. During flagellar propulsion, the head aligns along the oscillating magnetic fields with precision angle  $\varphi$ . Therefore, the small deformation of the two-tailed microrobot is approximated by

$$\kappa \frac{\partial^4 y_i}{\partial x^4}(x, t) + c_{n_i} \frac{\partial y_i}{\partial t}(x, t) = 0 \text{ for } i = 1, 2 \quad (3)$$

where  $y_i(x, t)$  is the deformation of the  $i$ th flexible tail, relative to a fixed frame of reference  $(\mathbf{e}_1(t), \mathbf{e}_2(t))$ , where  $\mathbf{e}_1(t)$  and  $\mathbf{e}_2(t)$  are orthonormal vectors such that  $\mathbf{e}_1(t)$  is oriented along the long axis of the head. Equation (3) describes the behavior of the two-tailed microrobot under the fluid-air interface and on the interface for relatively large distance to a nearby surface. On this interface, the average surface tension force exerted on the microrobot is zero along the transverse direction of the microrobot

and the microbeads. Therefore, the dynamics of the microrobot is governed by the balance between the magneto-elastic [first term in (3)] and drag [second term in (3)] forces. A periodic magnetic torque  $(\mathbf{M} \times \mathbf{B})$  enables the head to align along magnetic field lines. Therefore, the contribution of the magnetic torque to (3) is included by specifying the boundary conditions. At the left boundary,  $x = -l_1 - a$ , the tip of the first ultrathin tail is free from external forces and torques. Therefore,  $\frac{\partial^2 y_1}{\partial x^2}(-l_1 - a, t) = 0$  and  $\frac{\partial^3 y_1}{\partial x^3}(-l_1 - a, t) = 0$ . At the center,  $x = \pm a$ , the head is free to oscillate, and hence  $y_i(\pm a, t) = \pm a \sin \varphi \sin \omega_r t$  and  $\frac{\partial y_i}{\partial x}(\pm a, t) = \tan \varphi \sin \omega_r t$ , for  $i = 1, 2$ , where  $\omega_r$  is the angular velocity of the head. At the right boundary,  $x = l_2 + a$ , again the tip of the second tail is free from external forces and torques. Therefore,  $\frac{\partial^2 y_2}{\partial x^2}(l_2 + a, t) = 0$  and  $\frac{\partial^3 y_2}{\partial x^3}(l_2 + a, t) = 0$ . In (3),  $c_{n_i}$  is the following normal drag coefficient of the  $i$ th tail [24]:

$$c_{n_i} = 4\pi\eta / \left( \ln \left( \frac{l_i}{r_{t_i}} \right) + 0.193 \right). \quad (4)$$

As a consequence of the symmetric flagellar beat, the resulting averaged propulsive force of each tail will cancel out and the microrobot will achieve negligible motion regardless to the actuation frequency of the periodic magnetic field. A rotating magnetic field will enable the microrobot to rotate without swimming, as shown in Fig. 1. In order to achieve flagellar propulsion, the tail length ratio ( $r = l_1/l_2$ ) should be greater than one. The difference between the tails in length provides nonzero propulsive force that results in forward propulsion. The total propulsive force along the propulsion axis ( $\mathbf{e}_1(t)$ ) of the  $i$ th tail is given by [25]

$$F_i = \int_0^{l_i} \left( (c_{n_i} - c_{t_i}) v_{y_i} \frac{dy_i}{dx} - c_{t_i} v_{x_i} \right) dx \quad (5)$$

where  $v_{y_i}$  and  $v_{x_i}$  are the lateral and forward velocities of a segment along the  $i$ th tail, respectively. Further,  $c_{t_i}$  is the tangential drag coefficient of the  $i$ th tail and given by [24]

$$c_{t_i} = 2\pi\eta / \left( \ln \left( \frac{l_i}{r_{t_i}} \right) - 0.807 \right). \quad (6)$$

The net propulsive force ( $F_1 - F_2$ ) of two identical tails (in length, diameter, and stiffness) is zero based on (5). Therefore, microrobots with tail length ratio,  $1 < r < 2$ , are used to achieve noncontact manipulation of the microbeads owing to their ability to swim toward the desired object to be manipulated. They can also reverse their swimming direction to move away from the manipulated microbead using the second tail. The implication of having two tails is that the microrobot can swim along two opposite directions based on the actuation frequency of the external magnetic fields [26]. The swimming speed of the microrobot is calculated based on the following force balance between the tails and head:

$$\sum_{i=1}^2 F_i = 6\pi\eta(ab^2)^{1/3}v_x. \quad (7)$$

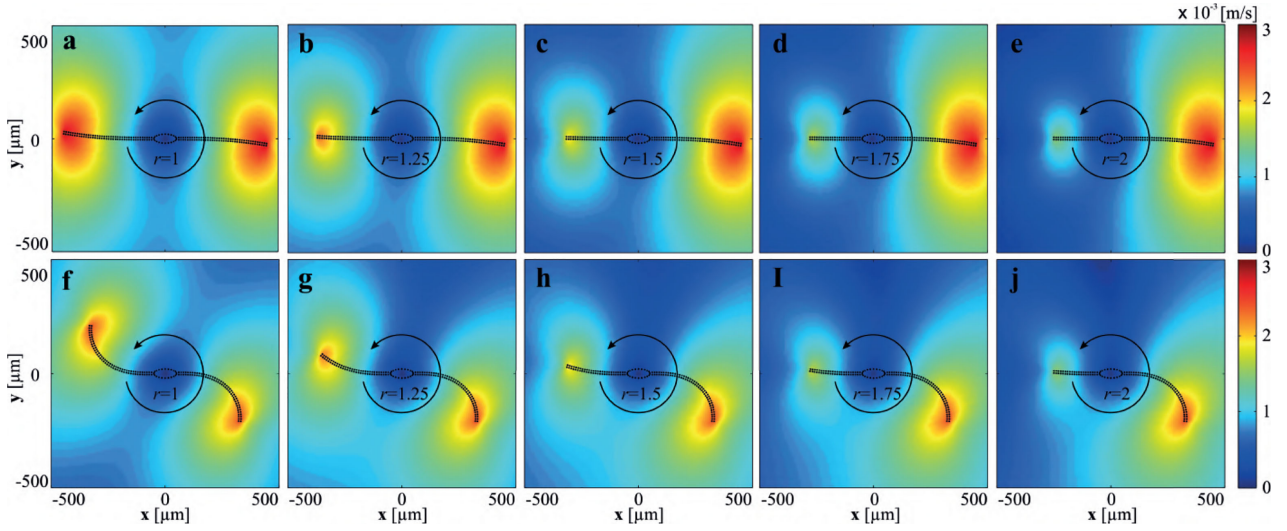


Fig. 2. Two-tailed microrobot induces a flow-field during rotation under the influence of a rotating magnetic field. The flow-field is calculated using (9) and (11) for  $2a = 50 \mu\text{m}$ ,  $b = 20 \mu\text{m}$ ,  $2r_t = 5 \mu\text{m}$ , and  $\eta = 0.95 \text{ Pa}\cdot\text{s}$ . (a)–(e) Flow-fields of two-tailed rigid microrobots are calculated for tail length ratios of 1, 1.25, 1.5, 1.75, and 2. (f)–(j) Flow-fields of two-tailed flexible microrobots (modulus of elasticity of 0.54 GPa) are calculated for tail length ratios of 1, 1.25, 1.5, 1.75, and 2. The flow-field created by the rigid microrobots is slightly higher than the flow-field of the soft microrobot regardless to the tail length ratio.

The drag torques exerted on the head and the tails of the microrobot are also balanced with the magnetic torque as follows:

$$\eta \left( F_r \omega_r + \sum_{i=1}^2 F_i \omega_i \right) = -\mathbf{M} \times \mathbf{B}(\mathbf{p}) \quad (8)$$

where  $F_r$  and  $F_i$  are the shape factors for the head and the  $i$ th tail which depend only on the geometry, respectively. Further,  $\omega_r$  is the angular velocity of the head with respect to a fixed frame of reference (see Fig. 1), and  $\omega_i$  is the relative angular velocity of the  $i$ th tail with respect to the head.

Equation (3) is only valid for small deformation  $y(x, t)$ . These deformations are observed only during flagellar propulsion using oscillating magnetic fields. However, rotating magnetic fields result in relatively large tail deformations, and hence the tangent angle,  $\phi(s, t) = dy(x, t)/dx$ , is used to characterize the deformation locally as a function of the arc length  $s$  instead of  $y(x, t)$ . Therefore, the governing equation is given by [27]

$$\kappa \frac{\partial^4 \phi_i}{\partial s^4}(s_i, t) + c_{ni} \frac{\partial \phi_i}{\partial t}(s_i, t) = 0 \text{ for } i = 1, 2 \quad (9)$$

where  $0 \leq s_i \leq l_i$ , is the arc length of the  $i$ th tail. The deformation of the  $i$ th tail is calculated using

$$\begin{pmatrix} x_{f_i}(s_i, t) \\ y_{f_i}(s_i, t) \end{pmatrix} = \begin{pmatrix} x_{f_i}(0, t) + \int_0^{s_i} \cos \phi(s_i, t) ds \\ y_{f_i}(0, t) + \int_0^{s_i} \sin \phi(s_i, t) ds \end{pmatrix} \text{ for } i = 1, 2 \quad (10)$$

where  $x_{f_i}(s_i, t)$  and  $y_{f_i}(s_i, t)$  are the coordinates of the  $i$ th tail, and  $x_{f_i}(0, t)$  and  $y_{f_i}(0, t)$  are the position of the point of attachment between the head and the  $i$ th tail. Similarly to flagellar propulsion, the contribution of the magnetic torque to (9) is induced by specifying the boundary conditions. At the head boundary,  $\phi_i(0, t) = \alpha(t) = 2\pi f_r t$  and  $\partial \phi_i(0, t)/\partial s = 0$ , where  $f_r$  is the rotation frequency of the microrobot. At the left and right boundaries, the tip of the tails are free from external forces ( $\partial^2 \phi_1(l_1, t)/\partial s^2 = 0$  and  $\partial^2 \phi_2(l_2, t)/\partial s^2 = 0$ )

and torques ( $\partial^3 \phi_1(l_1, t)/\partial s^3 = 0$  and  $\partial^3 \phi_2(l_2, t)/\partial s^3 = 0$ ). The governing equations are solved numerically to study the noncontact manipulation of the microbeads.

### B. Numerical Scheme of the Hydrodynamic Model

The flow-field is determined based on the method of regularized Stokeslets to provide a solution of the linear Stokes equations (1) and (2). The surface of the two-tailed microrobot and the surrounding microbeads are covered with  $N_s$  stokeslets boundary points. The velocity field, due to force  $\mathbf{f}_k$  at points  $\mathbf{x}_k$ , is given by [22]

$$\begin{aligned} \mathbf{u}(\mathbf{x}) = & \sum_{k=1}^{N_s} \frac{-\mathbf{f}_k}{2\pi\eta} \left[ \ln(\xi + \epsilon) - \frac{\epsilon(\xi + 2\epsilon)}{(\xi + \epsilon)\xi} \right] \\ & + \frac{1}{4\pi\eta} [\mathbf{f}_k \cdot (\mathbf{x} - \mathbf{x}_k)] (\mathbf{x} - \mathbf{x}_k) \left[ \frac{\xi + 2\epsilon}{(\xi + \epsilon)^2 (r_k^2 + \epsilon^2)^{1/2}} \right], \end{aligned} \quad (11)$$

where  $\xi = \sqrt{r_k^2 + \epsilon^2}$ , and  $r_k = |\mathbf{x} - \mathbf{x}_k|$ .  $\epsilon$  is a parameter that describes the sharpness of a delta-function and is calculated by,  $\epsilon = 0.25\Delta s \simeq 0.25\Delta s$ , and  $\Delta s = 2r_t$ . This delta function approximates the forces exerted by the beating tail on the fluid. The deformation of the tail and the drag forces are determined using finite-difference discretization of (3) and (9) for flagellar propulsion and rotation, respectively. The tail of the soft two-tailed microrobot is discretized into  $N \simeq 100$ , equally spaced mesh nodes. The partial differential equations (3) and (9) are solved numerically, and the time-dependent trajectory of the soft microrobotic sperm is calculated by forward Euler integration over consecutive time-steps of  $\Delta t \simeq 1 \times 10^{-3}$  seconds. The following steps are implemented to predict the behavior of the two-tailed microrobot and the orbiting microbeads.

- 1) The time-dependent deformation of the tails is calculated based on (3) and (9) for flagellar propulsion and rotation,

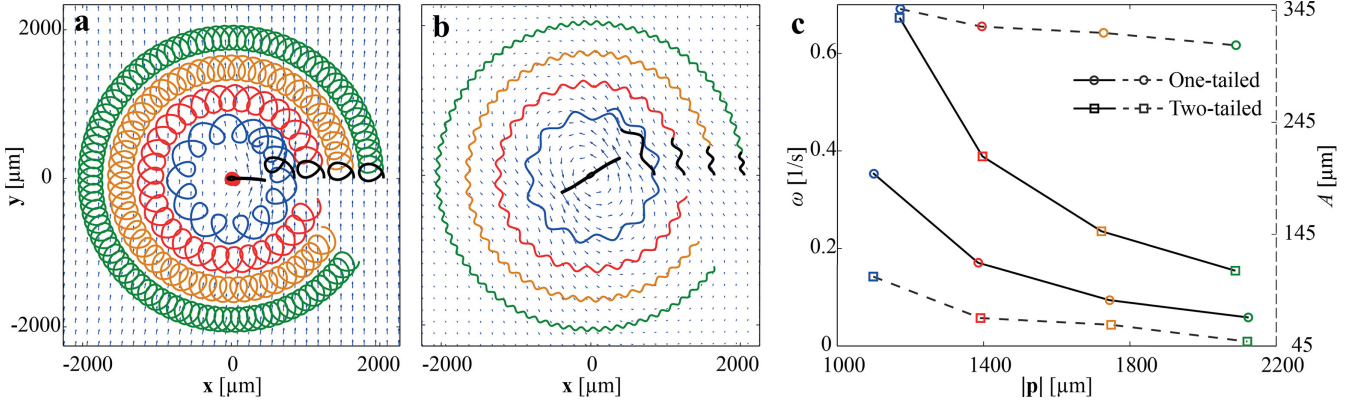


Fig. 3. Trajectories and averaged angular velocities of the orbiting microbeads are simulated for one- and two-tailed soft microrobots. The microbeads follow sprocketlike trajectories, and the black curves indicate the trajectories associated with the first complete cycle of the microrobot. The arrows indicate the flow-field at single time instant. The trajectories, flow-fields, and angular velocity are calculated using (9) and (11) for  $2a = 50 \mu\text{m}$ ,  $b = 20 \mu\text{m}$ ,  $2r_t = 5 \mu\text{m}$ , and  $\eta = 0.95 \text{ Pa}\cdot\text{s}$ . (a) Four microbeads at distances of  $1100$ ,  $1400$ ,  $1700$ , and  $2100 \mu\text{m}$  to one-tailed microrobot are influenced by its flow field. (b) Four microbeads at distances of  $1100$ ,  $1400$ ,  $1700$ , and  $2100 \mu\text{m}$  to two-tailed microrobot are influenced by its flow field. (c) Angular velocities ( $\omega$ ) of four microbeads and the amplitude ( $A$ ) of the sprocketlike trajectories are calculated versus the distance to the microrobot and indicate that the additional tail increases angular velocity of the orbiting microbeads. The angular velocity of microbeads orbiting a two-tailed microrobot is twice the velocity of microbeads orbiting single-tailed microrobot.

respectively, and for oscillating and rotating magnetic field inputs.

- 2) The velocities of approximately 100 points along the two-tailed microrobot are numerically calculated.
- 3) Forces at the Stokeslets boundary points are determined using inverse of (11) based on the calculated velocities along the microrobot.
- 4) Translational velocity of the two-tailed microrobot is calculated such that the sum of all forces at the Stokeslets points of the microrobot is zero.
- 5) Velocities of the microbeads are determined using (11) for the previously calculated forces.

Fig. 2 shows the flow-field created by rotating two-tailed microrobots with tail length ratio,  $1 \leq r \leq 2$ . In the case of rigid tails [see Fig. 2(a)–(e)], relatively high flow-fields are observed at the right and left boundaries of the tails for  $r = 1$ . As the tail length ratio increases, the flow-field created by the longer tail becomes dominant. These microrobots provide flow-fields that are capable of rotating the microbeads. However, they cannot swim owing to their rigidity [29]. In the case of flexible tails [see Fig. 2(f)–(j)], we observe a slight decrease in the velocity of the fluid with respect to the center of the rotating two-tailed microrobot compared to the rigid microrobots. Similarly, symmetric and asymmetric flow-fields are created by the rotating microrobots for  $r = 1$  and  $1.25 \leq r \leq 2$ , respectively. The implication of having two-tails with unequal length is that the head achieves periodic roto-translations due to the asymmetric flow-field of the tails. In the case of  $r = 1$ , the microrobot achieves pure rotations for rigid and flexible tails, as shown in Fig. 2(a) and (f), respectively.

One-tailed microrobots are also capable of allowing microbeads to orbit and they can also swim along one direction with a beating flexible tail. However, the additional tail increases the angular velocity of the orbiting microbeads. Fig. 3 provides a comparison between the response of one- and two-tailed microrobots at frequency of 1 Hz. Positions of four microbeads

are calculated at distances of  $1100$ ,  $1400$ ,  $1700$ , and  $2100 \mu\text{m}$  to one- and two-tailed microrobots, as shown in Fig. 3(a) and (b). For  $|\mathbf{p}_1| = 1100 \mu\text{m}$ , the angular velocities of the microbead are  $0.35 \text{ s}^{-1}$  and  $0.67 \text{ s}^{-1}$  for the one- and two-tailed microrobots, respectively. The angular velocity and the amplitude ( $A$ ) of the sprocketlike trajectories of the microbeads decrease as the distance to the microrobots increases, as shown in Fig. 3(c). For  $|\mathbf{p}_4| = 2100 \mu\text{m}$ , the one- and two-tailed microrobots allow the fourth microbead to orbit at angular velocities of  $0.05 \text{ s}^{-1}$  and  $0.15 \text{ s}^{-1}$ , respectively. Therefore, this simulation result indicates that the additional tail increases the angular velocity of the orbiting microbeads by at least a factor of 2. In addition, the additional tail decreases the peak-to-peak amplitude of the sprocketlike trajectory taken by the orbiting microbeads. In the case of one-tailed microrobot [see Fig. 3(a)], a microbead at distance of  $1100 \mu\text{m}$  orbits with a peak-to-peak amplitude of  $350 \mu\text{m}$ , whereas in the case of two-tailed microrobot [see Fig. 3(b)] the peak-to-peak amplitude decreases to  $100 \mu\text{m}$ .

In a second series of simulations, we analyze the path taken by the orbiting microbeads for rotating rigid two-tailed microrobots with tail length ratio,  $1 \leq r \leq 2$ , as shown in Fig. 4. The microrobot is allowed to rotate at frequency of 1 Hz, and the path taken by the microbead is calculated using (11) versus the distance to the microrobot  $\mathbf{p}_i$ . For  $r = 1$ , the microbeads follow sprocketlike trajectories and the angular velocity and amplitude ( $A$ ) of the  $i$ th microbead decrease with the increasing distance to the microrobot, as shown in Fig. 4(f) and (g), respectively. A similar response is observed for the case of flexible two-tailed microrobots with the same range of tail length ratio (see Fig. 5). Even though rigid microrobots achieves relatively higher angular velocities compared to flexible microrobots, manipulation of the microbead is achieved using the flexible microrobot owing to their ability to swim. Flexible microrobots with tail length ratio  $r = 1$  and  $r \gg 2$  are not also used to achieve noncontact manipulation. In the case of  $r = 1$ , the flexible tails produce negligible net translation as their propulsive forces cancel out.

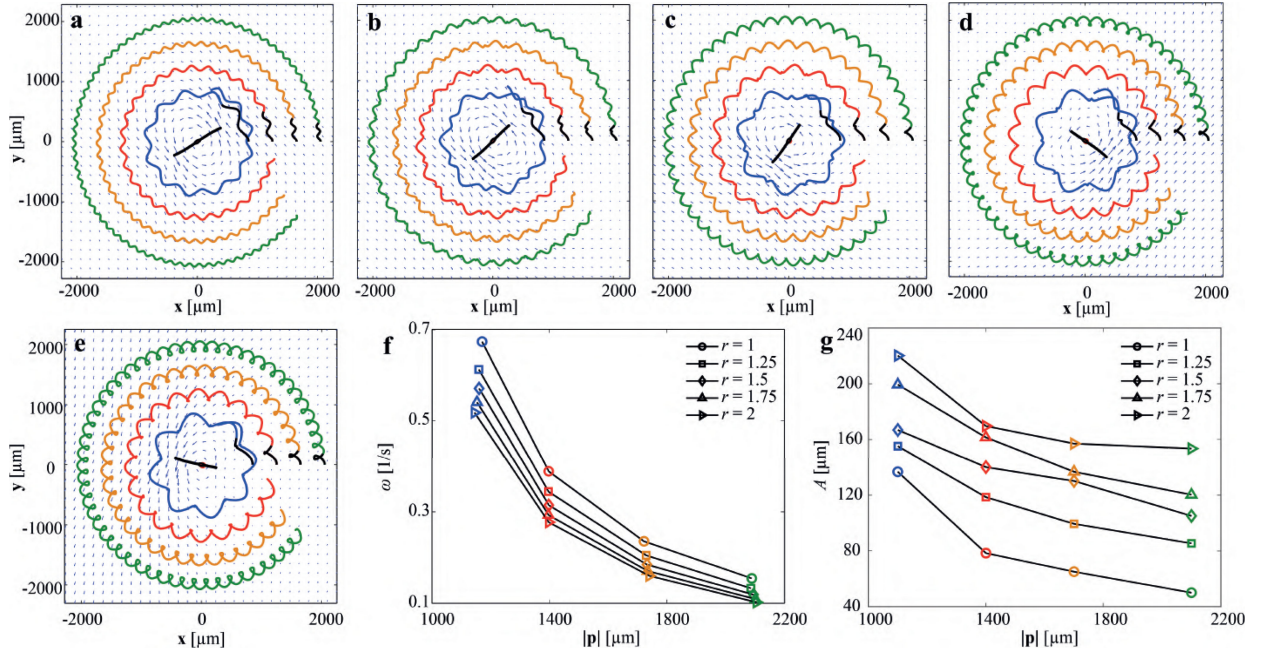


Fig. 4. Trajectories and averaged angular velocities of microbeads are simulated for two-tailed rigid microrobots with tail length ratio of  $1 \leq r \leq 2$ . The microbeads follow a sprocketlike trajectories, and the black curves indicate the trajectories associated with the first complete cycle of the microrobot. The arrows indicate the flow-field at single time instant. The microrobot rotates at frequency of 1 Hz and the  $i$ th microbead orbits at angular velocity  $\omega_i$  at distance  $p_i$  to the center of rotation. The trajectories, flow-fields, and angular velocity are calculated using (9) and (11) for  $2a = 50 \mu\text{m}$ ,  $b = 20 \mu\text{m}$ ,  $2r_t = 5 \mu\text{m}$ , and  $\eta = 0.95 \text{ Pa}\cdot\text{s}$ . (a) For  $r = 1$ ,  $\omega_1 = 0.67 \text{ s}^{-1}$  at  $|p_1| = 1100 \mu\text{m}$ . (b) For  $r = 1.25$ ,  $\omega_1 = 0.61 \text{ s}^{-1}$  at  $|p_1| = 1100 \mu\text{m}$ . (c) For  $r = 1.5$ ,  $\omega_1 = 0.57 \text{ s}^{-1}$  at  $|p_1| = 1100 \mu\text{m}$ . (d) For  $r = 1.75$ ,  $\omega_1 = 0.54 \text{ s}^{-1}$  at  $|p_1| = 1100 \mu\text{m}$ . (e) For  $r = 2$ ,  $\omega_1 = 0.51 \text{ s}^{-1}$  at  $|p_1| = 1100 \mu\text{m}$ . (f) Angular velocity decreases with the distance to the rotating microrobot and its tail length ratio. (g) Amplitude ( $A$ ) of the sprocketlike trajectories decreases with the distance to the microrobot ( $p$ ) and increases with the tail length ratio ( $r$ ).

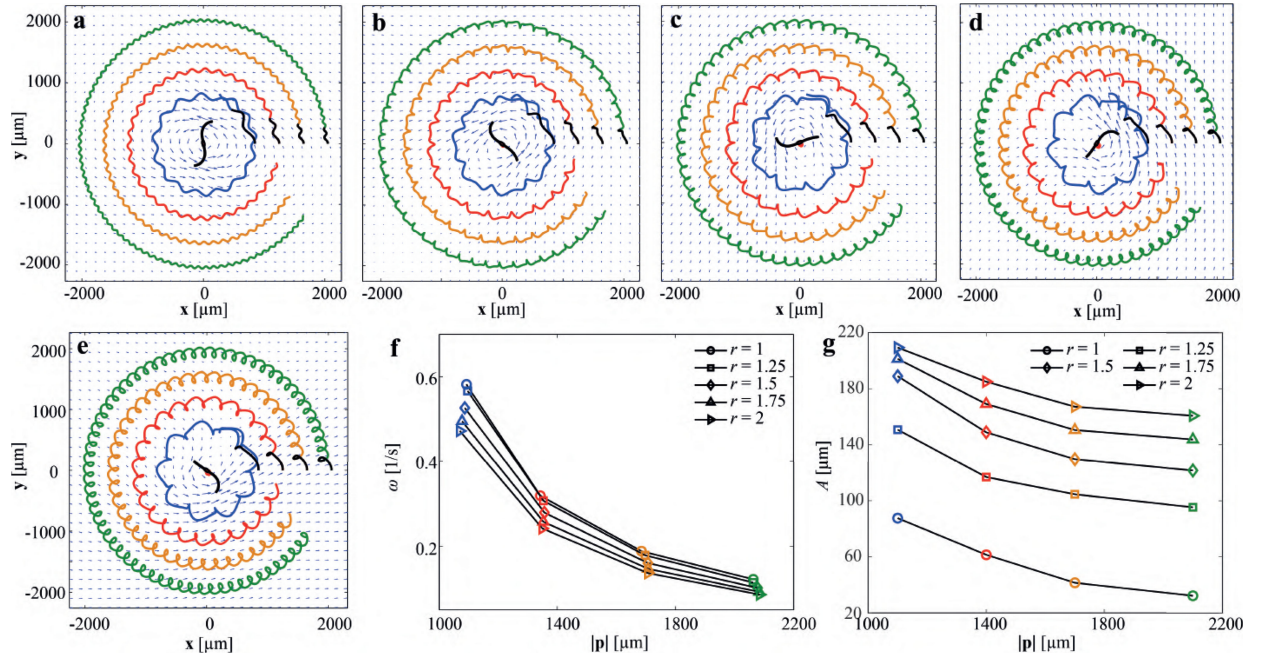


Fig. 5. Trajectories and averaged angular velocities of microbeads are simulated for soft two-tailed microrobots with tail length ratio of  $1 \leq r \leq 2$ . The microbeads follow a sprocketlike trajectories, and the black curves indicate the trajectories associated with the first complete cycle of the microrobot. The arrows indicate the flow-field at single time instant. The microrobot rotates at frequency of 1 Hz and the  $i$ th microbead orbits at angular velocity  $\omega_i$  at distance  $p_i$  to the center of rotation. The trajectories, flow-fields, and angular velocity are calculated using (9) and (11) for  $2a = 50 \mu\text{m}$ ,  $b = 20 \mu\text{m}$ ,  $2r_t = 5 \mu\text{m}$ , and  $\eta = 0.95 \text{ Pa}\cdot\text{s}$ . (a) For  $r = 1$ ,  $\omega_1 = 0.58 \text{ s}^{-1}$  at  $|p_1| = 1100 \mu\text{m}$ . (b) For  $r = 1.25$ ,  $\omega_1 = 0.56 \text{ s}^{-1}$  at  $|p_1| = 1100 \mu\text{m}$ . (c) For  $r = 1.5$ ,  $\omega_1 = 0.52 \text{ s}^{-1}$  at  $|p_1| = 1100 \mu\text{m}$ . (d) For  $r = 1.75$ ,  $\omega_1 = 0.49 \text{ s}^{-1}$  at  $|p_1| = 1100 \mu\text{m}$ . (e) For  $r = 2$ ,  $\omega_1 = 0.47 \text{ s}^{-1}$  at  $|p_1| = 1100 \mu\text{m}$ . (f) Angular velocity decreases with the distance to the rotating microrobot and its tail length ratio. (g) Amplitude ( $A$ ) of the sprocketlike trajectories decreases with the distance to the microrobot ( $p$ ) and increases with the tail length ratio ( $r$ ).

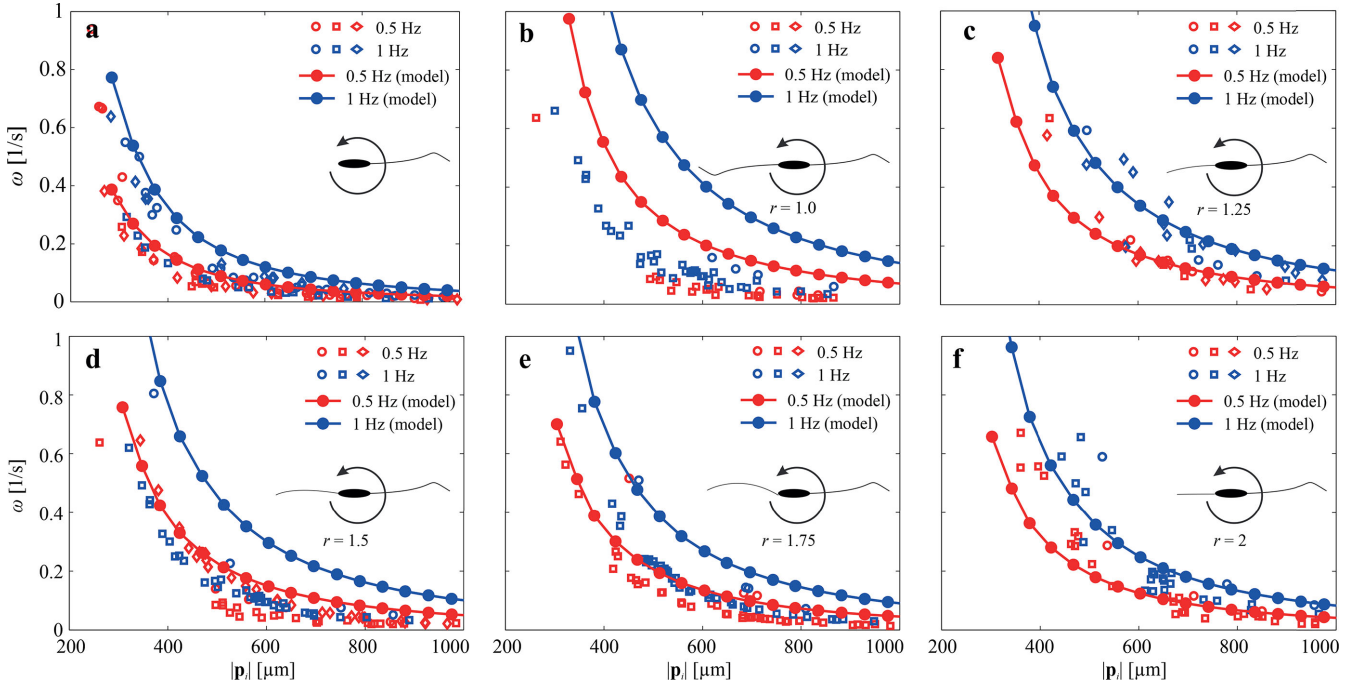


Fig. 6. Angular velocity of microbeads orbiting one- and two-tailed microrobots is characterized under the influence of a rotating magnetic field. The angular velocity of a microbead ( $\omega_i$ ) is measured at distance  $|p_i|$  to the center of rotation of a rotating microrobot. The average angular velocities, maximum, and minimum standard deviation (s.d.) are measured for 3 different microrobotic samples for each case (one- and two-tailed microrobots). The angular velocity (solid lines) is calculated using (9) and (11) for  $2a = 50 \mu\text{m}$ ,  $b = 20 \mu\text{m}$ ,  $2r_t = 5 \mu\text{m}$ , and  $\eta = 0.95 \text{ Pa}\cdot\text{s}$ . (a) Angular velocity of microbeads orbiting one-tailed microrobot ( $0.023 \leq \text{s.d.} \leq 0.66 \text{ s}^{-1}$ ). (b) Average  $\omega_i$  for  $r \approx 1.0$  ( $0.02 \leq \text{s.d.} \leq 0.19 \text{ s}^{-1}$ ). (c) Average  $\omega_i$  for  $r \approx 1.25$  ( $0.046 \leq \text{s.d.} \leq 0.93 \text{ s}^{-1}$ ). (d) Average  $\omega_i$  for  $r \approx 1.5$  ( $0.03 \leq \text{s.d.} \leq 0.93 \text{ s}^{-1}$ ). (e) Average  $\omega_i$  for  $r \approx 1.75$  ( $0.02 \leq \text{s.d.} \leq 0.68 \text{ s}^{-1}$ ). (f) Average  $\omega_i$  for  $r \approx 2.0$  ( $0.03 \leq \text{s.d.} \leq 0.84 \text{ s}^{-1}$ ). Please refer to the accompanying video.

In the second case of  $r \gg 2$ , the longer tail provides greater propulsive force than the short tail regardless to the actuation frequency, and does not enable the microrobot to swim back and forth to enhance the ability of the microrobot to swim away from the manipulation site.

### III. CHARACTERIZATION OF THE NONCONTACT MANIPULATION

Microbeads are allowed to orbit externally-actuated two-tailed microrobots and their response is characterized using an orthogonal configuration of electromagnetic coils.

#### A. System Description

Two-tailed microrobots are fabricated with tail length ratios of approximately 1.25, 1.5, 1.75, and 2 by electrospinning [28]. This fabrication technique provides continuous beaded-fibers of polystyrene with iron particles embedded into the beads. The modulus of elasticity of the microrobotic samples is measured using depth sensing indentation as  $0.54 \pm 0.054 \text{ GPa}$  [26]. The average minor and major diameter of the head are  $38 \pm 12 \mu\text{m}$  and  $101 \pm 31 \mu\text{m}$ , respectively, and the average tail diameter is  $10 \pm 4 \mu\text{m}$ . The microrobots are contained inside a cubic chamber with edge length of 40 mm. Polystyrene microbeads (PLA-M, plain, 12-00-304, Micromod Partikeltechnologie GmbH, Rostock-Warnemuende, Germany) with average diameter of  $30 \mu\text{m}$  are added to glycerin with viscosity of  $0.95 \text{ Pa}\cdot\text{s}$ . All experiments are conducted on the fluid-air interface to enable the microrobot and microparticles to lie on the same plane within a workspace of less than  $1 \times 1 \text{ mm}^2$ , whereas the surface area of

the chamber is  $4 \times 4 \text{ cm}^2$ . Therefore, the microrobots and the microbeads are not influenced by wall effects. This chamber is surrounded by four orthogonal electromagnetic coils. Each electromagnetic coil has an inner-, outer-diameter, and length of 20, 40, and 80 mm, respectively. The wire thickness is 0.7 mm and each coil has 3200 turns, and generates maximum magnetic field of 70 mT in the common center of the electromagnetic configuration. The positions of the two-tailed microrobot and the orbiting microbeads are observed using a microscopic unit (MF Series 176 Measuring Microscopes, Mitutoyo, Kawasaki, Japan), and videos are acquired using a camera (avA1000-120kc, Basler Area Scan Camera, Basler AG, Ahrensburg, Germany) and a  $10\times$  Mitutoyo phase objective.

#### B. Characterization of the Orbiting Microbeads

The microbeads are allowed to orbit one- and two-tailed microrobots under the influence rotating magnetic field at frequencies of 0.5 and 1 Hz. The distances between the microrobot and the microbeads are allowed to vary between trials. The angular velocities of the microrobot and microbeads are measured versus their distance. Fig. 6(a) shows the measured angular velocities of orbiting microbeads actuated via a rotating one-tailed microrobot. The angular velocities decays nearly as  $\sim |p_i|^{-2}$  away from the center of rotation of the microrobot. The influence of the rotation frequency also decays as the distance of the microbead to the microrobot increases. In the case of one-tailed microrobot, the microbeads rotate at an average angular velocity of  $0.03$  and  $0.08 \text{ s}^{-1}$  under the influence of

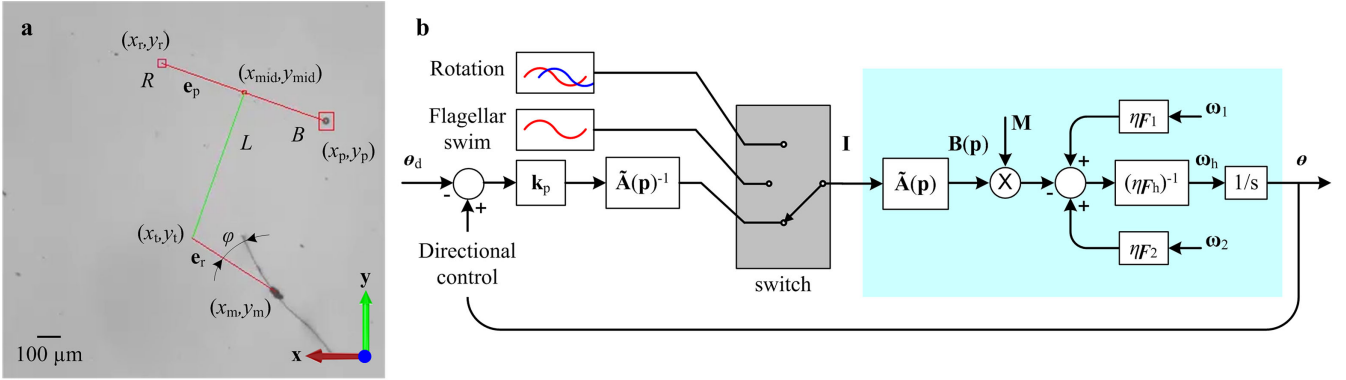


Fig. 7. Combination of oscillating and rotating magnetic fields is applied to achieve noncontact manipulation of the microbeads. (a) Positions of the microrobot  $(x_m, y_m)$  and the microbeads  $(x_p, y_p)$  are detected using a feature tracking algorithm. A vector from the initial position of the microbead to the target position  $(x_r, y_r)$  is calculated and a midpoint  $(x_{mid}, y_{mid})$  along segment  $RB$  is determined. The microrobot is controlled to swim toward a point along a vector perpendicular to  $RB$  and intersects with the midpoint. (b) Control is achieved using three inputs. The first input aligns the microrobot  $(\mathbf{e}_1(t))$  toward the reference position. The second control input provides uniform field with a sinusoidally varying orthogonal component to achieve flagellar propulsion. The third input provides rotating magnetic fields to rotate the microrobot and enable the microbead to orbit toward the reference trajectory.

rotating microrobot at frequencies of 0.5 and 1 Hz, respectively, at distance of approximately  $600 \mu\text{m}$  from the center of rotation of the microrobot [see Fig. 6(a)]. The angular velocity of the orbiting microbeads decreases as their distance to the rotating microrobot increases. For  $|\mathbf{p}_i| \approx 800 \mu\text{m}$ , the average angular velocities of the microbeads are measured as  $0.016$  and  $0.031 \text{ s}^{-1}$  for  $f_r = 0.5 \text{ Hz}$  and  $f_r = 1 \text{ Hz}$ , respectively.

Fig. 6(b)–(f) show the measured angular velocities of microbeads orbiting two-tailed microrobots with tail length ratio  $1 \leq r \leq 2$ . For  $r = 1$  and at  $|\mathbf{p}_i| \approx 600 \mu\text{m}$ , the angular velocities of the microbeads are measured as  $0.05$  and  $0.095 \text{ s}^{-1}$  for  $f_r = 0.5 \text{ Hz}$  and  $f_r = 1 \text{ Hz}$ , respectively [see Fig. 6(b)]. This measurement indicates that the additional tail increases the angular velocity of the microbeads by factors of 1.6 and 1.2 for actuation frequencies of 0.5 and 1 Hz, respectively. At  $|\mathbf{p}_i| \approx 800 \mu\text{m}$ , the angular velocity decreases to  $0.024 \text{ s}^{-1}$  and  $0.043 \text{ s}^{-1}$  for  $f_r = 0.5 \text{ Hz}$  and  $f_r = 1 \text{ Hz}$ , respectively. At this distance the angular velocity of microbeads orbiting two-tailed microrobots is greater than that of a microbead orbiting a single-tailed microrobot by a factor of 1.5 for  $f_r = 0.5 \text{ Hz}$ , while an increase by a factor of 1.4 is observed at  $f_r = 1 \text{ Hz}$ . Although the additional tail increases the angular velocity of the orbiting microbeads, microrobots with  $r = 1$  are not used to achieve non-contact manipulation owing to their inability to swim regardless to the actuation frequency of the external magnetic field.

Fig. 6(c) shows the angular velocities of microbeads orbiting microrobots with  $r = 1.25$ . Microrobots with this tail length ratio achieves negligible forward swim at  $f_r = 2.8 \pm 0.9 \text{ Hz}$ , and undergo flagellar swim using its long and short tail below and above this reversal frequency [31]. At  $|\mathbf{p}_i| \approx 600 \mu\text{m}$ , the angular velocities of the microbeads are measured as  $0.15 \text{ s}^{-1}$  and  $0.45 \text{ s}^{-1}$  for  $f_r = 0.5 \text{ Hz}$  and  $f_r = 1 \text{ Hz}$ , respectively. As the distance to the rotating microrobot increases to  $800 \mu\text{m}$ , the angular velocities decreases by factors of 1.8 and 2.3 for  $f_r = 0.5 \text{ Hz}$  and  $f_r = 1 \text{ Hz}$ , respectively. Fig. 6(d) shows the response of the microbeads to the rotation of two-tailed microrobot with  $r = 1.5$ . Similarly to microrobot with  $r = 1.25$ , microrobots with this ratio can achieve flagellar swim using the

long and short tails below and above actuation frequency of  $5.4 \pm 0.7 \text{ Hz}$ . At  $|\mathbf{p}_i| \approx 600 \mu\text{m}$ , the angular velocities are measured as  $0.04 \text{ s}^{-1}$  and  $0.095 \text{ s}^{-1}$  for  $f_r = 0.5 \text{ Hz}$  and  $f_r = 1 \text{ Hz}$ , respectively. The angular velocities decrease to  $0.024 \text{ s}^{-1}$  and  $0.043 \text{ s}^{-1}$  at  $|\mathbf{p}_i| \approx 800 \mu\text{m}$  and for  $f_r = 0.5 \text{ Hz}$  and  $f_r = 1 \text{ Hz}$ , respectively. Finally, microrobots with  $r = 1.75$  can also achieve flagellar swimming below and above actuation frequency of  $10.4 \pm 0.5 \text{ Hz}$  and are used in micromanipulation owing to its ability to swim back and forth. Fig. 6(e) shows the response of microbeads actuated without contact using microrobots with this tail length ratio. At  $|\mathbf{p}_i| \approx 600 \mu\text{m}$ , the angular velocities of the orbiting microbeads are measured as  $0.08$  and  $0.13 \text{ s}^{-1}$  for  $f_r = 0.5 \text{ Hz}$  and  $f_r = 1 \text{ Hz}$ , respectively. Again, the angular velocity decreases to  $0.031 \text{ s}^{-1}$  and  $0.052 \text{ s}^{-1}$  at  $|\mathbf{p}_i| \approx 800 \mu\text{m}$  for  $f_r = 0.5 \text{ Hz}$  and  $f_r = 1 \text{ Hz}$ , respectively.

Similarly to one-tailed microrobots, two-tailed microrobots with tail length ratio of 2 swim along one direction regardless to the actuation frequency. The response of the microbeads to the rotation of two-tailed microrobot with  $r = 2$  is shown in Fig. 6(f). At  $|\mathbf{p}_i| \approx 600 \mu\text{m}$ , the angular velocities of the orbiting microbeads are measured as  $0.15 \text{ s}^{-1}$  and  $0.35 \text{ s}^{-1}$  for  $f_r = 0.5 \text{ Hz}$  and  $f_r = 1 \text{ Hz}$ , respectively. Again, the angular velocity decreases to  $0.05$  and  $0.07 \text{ s}^{-1}$  at  $|\mathbf{p}_i| \approx 800 \mu\text{m}$  and for  $f_r = 0.5 \text{ Hz}$  and  $f_r = 1 \text{ Hz}$ , respectively. Our characterization results show qualitative and quantitative agreement between the experimental results and the theoretical prediction of the model. The deviations between the experimental results and simulations [evident in Fig. 6(b)] are attributed to errors in some of the parameters that enter the model such as the magnetization, dimensions, and bending stiffness of the two-tailed microrobots. The deviations between experiments and numerical model in the initial deformation of the tail decreases the accuracy of the calculated time-dependent sprocketlike trajectory and allows us to only achieve qualitative agreement between the actual path taken by the orbiting microbeads and theoretical predictions, as shown in Figs. 1, and 3–5. Nevertheless, the effect of these deviations on the positioning accuracy of the microbeads can be mitigated using feedback control.



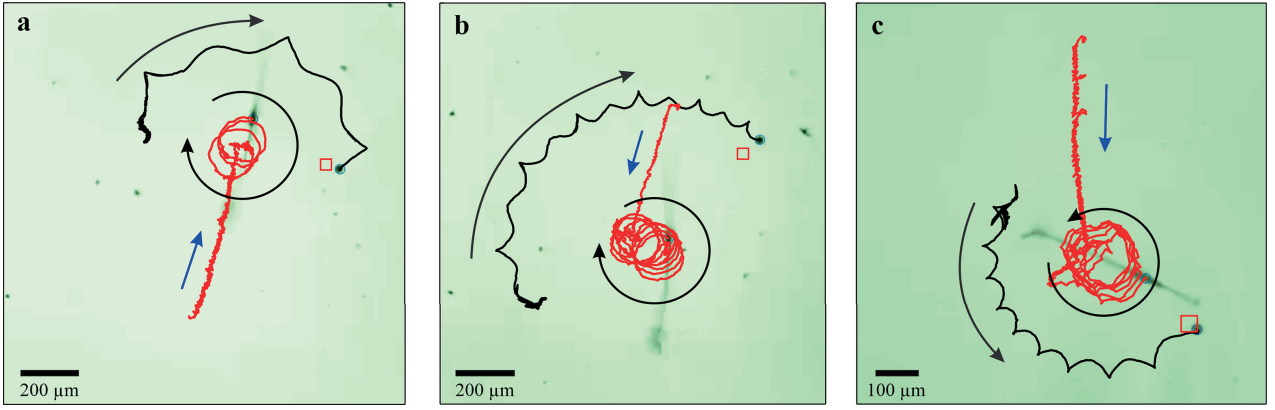


Fig. 8. Noncontact manipulation of microbeads is achieved using two-tailed microrobots. (a) Two-tailed microrobot (tail length ratio of 1.3) translates the microbead to the reference position with error of 45 and 15  $\mu\text{m}$  along  $x$ - and  $y$ -axis, respectively. (b) Microrobot (tail length ratio of 1.3) translates the microbead with position error of 26.2 and 48.7  $\mu\text{m}$  along  $x$ - and  $y$ -axis, respectively. (c) Microrobot (tail length ratio of 2.2) translates the microbead with position error of 15 and 11.2  $\mu\text{m}$  along  $x$ - and  $y$ -axis, respectively. The red and black lines represent the trajectories of the microrobot and the microbead, respectively, and the red square indicates the reference position. *Please refer to the accompanying video.*

#### IV. CLOSED-LOOP CONTROL OF NONMAGNETIC MICROBEADS

Our closed-loop control strategy is based on switching between flagellar propulsion and rotation. The former is necessary to swim toward or away from the microbead and the manipulation site, while the latter is required to enable the microbead to orbit the microrobot toward the reference position. The following steps are achieved to manipulate the microbead without contact. First, the microrobot swims toward a point between the microbead and the reference position. Second, rotating magnetic fields are applied to achieve non-contact manipulation. Third, the microrobot swims away from the microbead using flagellar propulsion. We determine the of the position of the microbead  $(x_p, y_p)$  and its desired position  $(x_r, y_r)$ . A perpendicular position vector  $\mathbf{L}$  is calculated from the midpoint  $(x_{\text{mid}}, y_{\text{mid}})$  of the line segment  $RB$  [see Fig. 7(a)]. The magnitude of this position vector defines a reference position  $(x_t, y_t)$  to the two-tailed microrobot [see Fig. 7(a)]. The magnitude of the position vector  $\mathbf{L}$  can be used to control the angular velocity of the orbiting microbead based on our characterization results (see Fig. 6). It can also be used to decrease the amplitude of the sprocketlike trajectories taken by the microbeads, as shown in Figs. 4(g) and 5(g). Directional control of the microrobot toward  $(x_t, y_t)$  is achieved using the following magnetic field [30]:

$$\mathbf{B}(\mathbf{p}) = \tilde{\mathbf{A}}(\mathbf{p})\mathbf{I} \quad (12)$$

where  $\tilde{\mathbf{A}}(\mathbf{p})$  and  $\mathbf{I}$  are the magnetic field-current map and the input current vector to the electromagnetic coils, respectively. We set the magnetic field in (12) to a proportional control input based on the orientation error ( $\mathbf{e}$ ) between  $\mathbf{e}_1(t)$  and the desired reference position,  $\mathbf{B}(\mathbf{p}) \Rightarrow \mathbf{k}_p \mathbf{e}$ , where  $\mathbf{k}_p$  is a diagonal positive-definite gain matrix and  $\mathbf{e}$  is a position error vector. The inverse of map (12) is used to provide the current input that aligns  $\mathbf{e}_1(t)$  toward the desired position, as shown in Fig. 7(b). Directional control of the microrobot toward point  $(x_t, y_t)$  is followed by oscillation of the magnetic field lines with an angle  $\varphi$  to achieve flagellar swimming. To switch between flagellar swimming to rotation, a threshold  $\varepsilon_r$  is set and compared to

TABLE I  
PSEUDOCODE OF THE NONCONTACT CLOSED-LOOP CONTROL OF THE MICROBEADS

---

**Inputs:** Reference position of the microbead  $(x_r, y_r)$ , reference position of the microrobot  $(x_t, y_t)$ , position of the microbead  $(x_p, y_p)$ , position of the microrobot  $(x_m, y_m)$ , precision angle ( $\varphi$ ), maximum current ( $I_{\text{max}}$ ), rotational frequency ( $f_r$ ), flagellar propulsion frequency ( $f_f$ ), distance ( $L$ ), error thresholds for the microbead and the microrobot ( $\varepsilon_p$  and  $\varepsilon_r$ ).

**Outputs:** Input currents to the coils ( $I_1, I_2, I_3$ , and  $I_4$ ).

```

while |e_p| > ε_p do
    x_mid = (x_r + x_p) / 2 ; p r_x = |x_r - x_p|
    y_mid = (y_r + y_p) / 2 ; p r_y = |y_r - y_p|
    p r = [p r_x  p r_y]^T ; v = [p r_y  -p r_x]^T
    v_hat = v / ||v|| ; L = L v
    x_t = x_mid ± L v_hat_x ; y_t = y_mid ∓ L v_hat_y
    e_r = [x_m  y_m]^T - [x_t  y_t]^T
    θ = cos-1(θ_r_y / |θ_r|)
    if |e_r| > ε_r
        θ_osc = θ + φ ; φ = -φ
        [I1,3  I2,4]T = I_max [cos(θ_osc)  sin(θ_osc)]T
    end
    e_p = [x_p  y_p]^T - [x_r  y_r]^T
    if |e_p| > ε_p
        [I1,3  I2,4]T = I_max [cos(2π f_r t)  sin(2π f_r t)]T
    end
    if |e_p| ≤ ε_p && |e_r| ≤ ε_r
        θ_osc = θ + φ + 90° ; φ = -φ
        [I1,3  I2,4]T = I_max [cos(θ_osc)  sin(θ_osc)]T
    end
end
    
```

---

the following position error ( $\mathbf{e}_r$ ) between point  $(x_t, y_t)$  and the position of the microrobot  $(x_m, y_m)$ :

$$\mathbf{e}_r = [x_m \ y_m]^T - [x_t \ y_t]^T. \quad (13)$$

Rotational magnetic fields are applied when  $|\mathbf{e}_r| \leq \varepsilon_r$ . In this case, the microrobot follows the rotating field lines and the microbead orbits the microrobot toward the reference position. Another threshold ( $\varepsilon_p$ ) is compared to the error between the

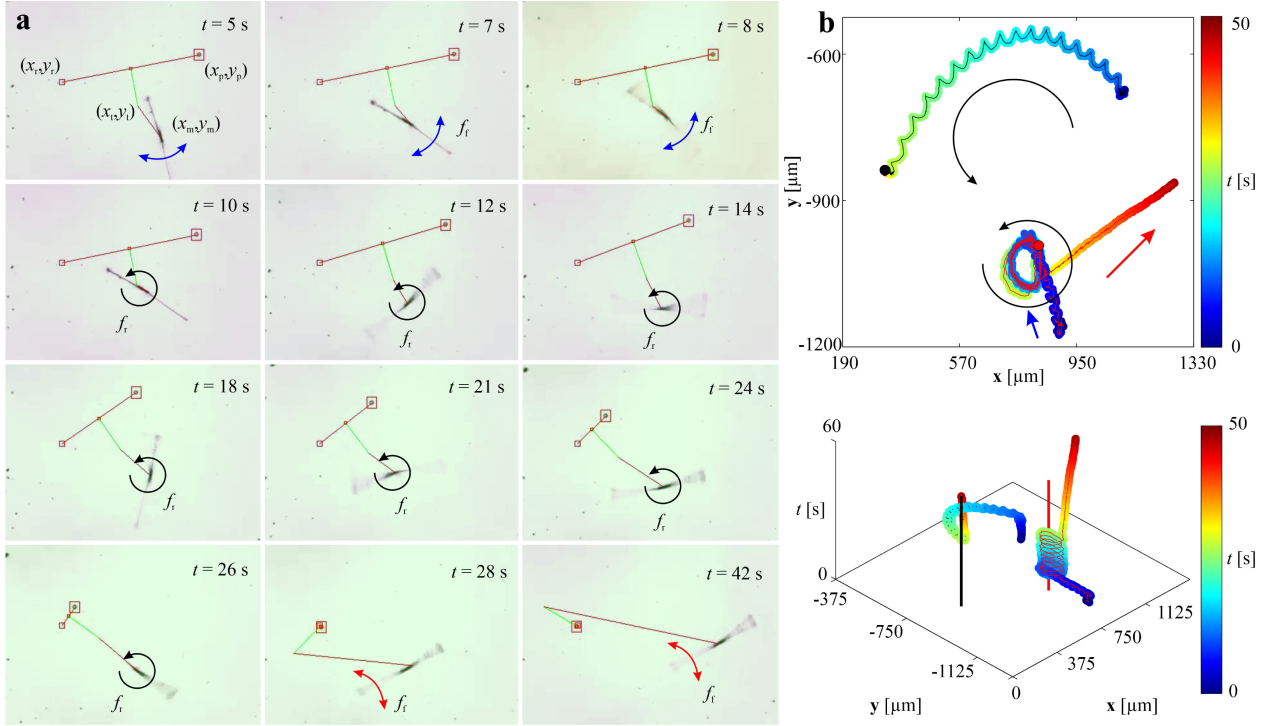


Fig. 9. Closed-loop control of a microbead via non-contact manipulation is achieved using a two-tailed microrobot with tail length ratio of 1.9. The large and small red squares indicate the microbead and the desired reference position, respectively. The red line represent the distance between the microbead and the target, and the green line indicate the distance between the center of rotation of the microrobot the midpoint along the segment between target and the microbead. (a) For  $t \leq 8$  s, the microrobot is controlled to swim toward a point the center of rotation under the influence of oscillating magnetic field at  $f = 2$  Hz. At time  $t \simeq 10$  s, the microrobot rotates at frequency of 1 Hz and the microbead orbits at an angular velocity of  $0.1 \text{ s}^{-1}$ . The microbeads is positioned at the reference position at  $t = 26$  s. At  $t > 26$  s, the microrobot switches back to flagellar propulsion and swims away at  $f_r = 8$  Hz. (b) Trajectories of the microbead and the microrobots indicate that the microbead is positioned at the reference position with error of 9 and  $7.5 \mu\text{m}$  along  $x$ - and  $y$ -axis, respectively. Please refer to the accompanying video.

position of the microbead and its target and given by

$$\mathbf{e}_p = [x_p \ y_p]^T - [x_r \ y_r]^T. \quad (14)$$

Again, we switch between rotating magnetic fields to oscillating magnetic fields when  $|\mathbf{e}_p| \leq \varepsilon_p$  to move away from the manipulation site of the microbead. A pseudocode of the closed-loop control implementation is provided in Table I.

Fig. 8(a) shows a representative control of a microbead toward a reference position (small red square). First, the microrobot (with  $r = 1.3$ ) swims and positions itself between the initial and desired positions of the microbead ( $L = 0 \mu\text{m}$ ). The microrobot swims at an average swimming speed of  $18.1 \mu\text{m/s}$  under the influence of oscillating magnetic fields at frequency of 5 Hz. Second, the microrobot starts to rotate to enable the microbead to orbit its center of rotation and approach the desired position (small red square). In this trial, the microbead orbits at an angular velocity of  $0.14 \text{ s}^{-1}$  and is positioned at the reference with position errors along  $x$ - and  $y$ -axis of  $45$  and  $15 \mu\text{m}$ , respectively. This noncontact manipulation is achieved in  $67.3$  s. Fig. 8(b) shows another representative trial with a microrobot with  $r = 1.3$ . The position errors are measured as  $26.2$  and  $48.7 \mu\text{m}$  along  $x$ - and  $y$ -axis, respectively. This noncontact manipulation is achieved in  $68.8$  s. A microrobot with  $r = 2.2$  achieves noncontact manipulation of a microbead with position errors of  $15$  and  $11.2 \mu\text{m}$  along  $x$ - and  $y$ -axis, respectively, as shown in Fig. 8(c). These closed-loop control trials (for  $L = 0 \mu\text{m}$ ) are repeated and the

average position error is  $52.5 \pm 23.4 \mu\text{m}$  ( $n = 10$ ). The rotational behavior of the two-tailed microrobots is attributed to the asymmetric flow-fields created by the different two tails in length. This asymmetric flow-field is even more evident in Fig. 8(c) owing to the relatively large tail length ratio ( $r = 2.2$ ) compared to tail length ratio of 1.3 [see Fig. 8(a) and (b)]. The positioning accuracy of the microbead is also limited due to the relatively large amplitude of the sprocketlike trajectory of the microbead. Our simulation and experimental results (see Figs. 3–5) suggest that increasing the distance between the orbiting microbeads and the rotating microrobot decreases the amplitude of the sprocketlike trajectory and the angular velocity of the microbeads with respect to the microrobot.

We set the distance between the center of rotation of the microrobot and the midpoint of the line segment  $RB$  to half body-length ( $L = (l_1 + l_2 + 2a)/2$ ). Our simulation results suggest that increasing  $L$  decreases the amplitude of the sprocketlike trajectories taken by the orbiting microbeads (see Fig. 5). Fig. 9(a) shows a two-tailed microrobot with tail length ratio of 1.9. Uniform magnetic fields are generated and oriented toward the center of rotation  $(x_t, y_t)$  of the microrobot using (12). These fields are oscillated with an angle  $\varphi = \pm 45^\circ$  at frequency of 2 Hz. The microrobot swims toward point  $(x_t, y_t)$  at an average speed of  $41.7 \mu\text{m/s}$ . At  $t \simeq 8.6$  s, the condition  $|\mathbf{e}_r| \leq \varepsilon_r$  is satisfied and the rotating magnetic fields are generated at frequency of 1 Hz. We observe that the microbead starts to orbit

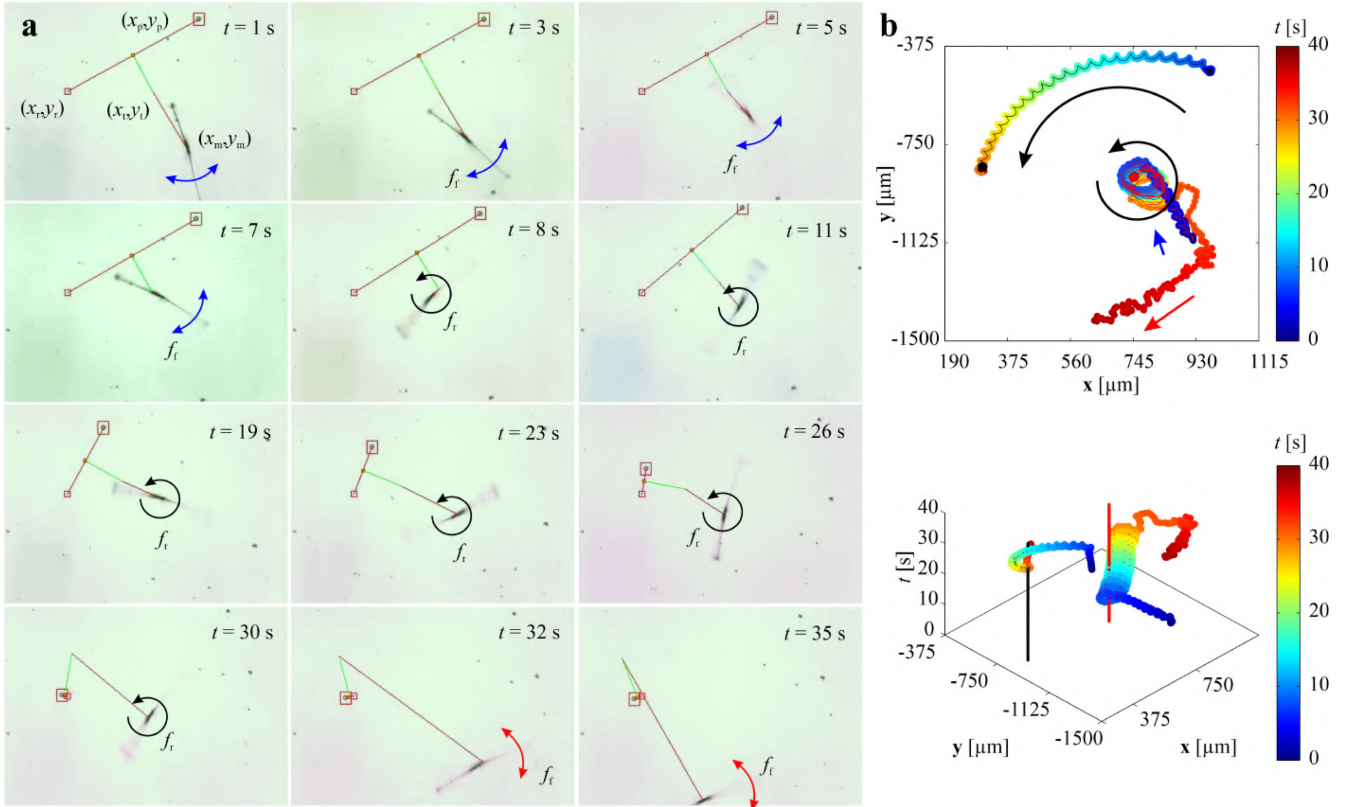


Fig. 10. Closed-loop control of a microbead via non-contact manipulation is achieved using a two-tailed microrobot with tail length ratio of 1.9. The large and small red squares indicate the microbead and the desired reference position, respectively. The red line represent the distance between the microbead and the target, and the green line indicate the distance between the center of rotation of the microrobot the midpoint along the segment between target and the microbead. (a) For  $t \leq 7$  s, the microrobot is controlled to swim toward a point the center of rotation under the influence of oscillating magnetic field at  $f = 2$  Hz. At  $t \simeq 8$  s, the microrobot rotates at frequency of 1 Hz and the microbead orbits at an angular velocity of  $0.1 \text{ s}^{-1}$ . The microbeads is positioned at the reference position at  $t = 30$  s. At  $t > 30$  s, the microrobot switches back to flagellar propulsion and swims away at  $f_r = 8$  Hz. (b) Trajectories of the microbead and the microrobots indicate that the microbead is positioned at the reference position with error of 18.75 and 11.25  $\mu\text{m}$  along  $x$ - and  $y$ -axis, respectively. Please refer to the accompanying video.

the rotating microrobot and follow a sprocketlike trajectory [see Fig. 9(b)] toward the reference position at an angular velocity of  $0.12 \text{ s}^{-1}$ . The control system switches back from rotating to oscillating magnetic fields when  $|\mathbf{e}_p| \leq \varepsilon_p$ , at  $t \simeq 27$  seconds. The microrobot is controlled to swim away from the microbead at frequency of 8 Hz and its speed is measured as  $23.8 \mu\text{m/s}$ . In this trial, the microbead is positioned at the reference position with error of 9 and  $7.5 \mu\text{m}$  along  $x$ - and  $y$ -axis, respectively.

Fig. 10(a) shows another representative closed-loop control trial of a microbead using a two-tailed microrobot with tail length ratio of 1.9. The microrobot is controlled to swim toward the center of rotation, rotate, and swim away at frequencies of 8, 1 (rotation frequency), and 2 Hz, respectively. We observe that the flow-field created during flagellar propulsion decreases with the beating frequency. Therefore, relatively low actuation frequencies are used to swim toward the center of rotation, while relatively high frequencies are used to swim away to decrease the influence of the flow-field on the microbead after the manipulation. In this trial, the microrobot is controlled to swim toward the center of rotation at an average speed of  $63.5 \mu\text{m/s}$  under the influence of oscillating magnetic fields of 2 Hz. At  $t \simeq 8$  seconds, rotating fields are applied at frequency

of 1 Hz and the microbead orbits at an angular velocity of  $0.1 \text{ s}^{-1}$ . At  $t \simeq 32$  s, oscillating magnetic fields are applied at frequency of 8 Hz and the microrobot swims away at average speed of  $40.8 \mu\text{m/s}$  [see Fig. 10(b)]. The errors along  $x$ - and  $y$ -axis are measured as 18.75 and  $11.25 \mu\text{m}$ , respectively. In this case ( $L = (l_1 + l_2 + 2a)/2$ ), the maximum position error is  $21.8 \mu\text{m}$ . Please refer to the accompanying video.

Table II provides the closed-loop control characteristics for the cases of  $L = 0$  and  $L = 0.5$  body-length. The position error between the microbead and the reference position decreases with the distance ( $L$ ) between the midpoint along the segment  $RB$  and the center of rotation of the two-tailed microrobot, while the angular velocity of the orbiting microbeads increases as its distance to the center of the microrobot is decreased. Therefore, there exist a tradeoff between the positioning accuracy of the microbeads and the manipulation time (angular velocity of the microbead). This tradeoff is controlled by the distance between the center of rotation and the midpoint of the segment between the target position and the initial position of the microbead. It is also possible to understand the influence of the distance ( $L$ ) using the theoretical predictions of the numerical model. Figs. 4(g) and 5(g) show that as  $L$  increases the amplitude of the

TABLE II  
CLOSED-LOOP CONTROL CHARACTERISTICS OF THE MICROBEADS ARE CALCULATED FOR  $L = 0$  AND  $L = 0.5$  BODY-LENGTH (BL)

$L$ [ $\mu\text{m}$ ]	$e_x$ [ $\mu\text{m}$ ]	$e_y$ [ $\mu\text{m}$ ]	$e$ [ $\mu\text{m}$ ]	$\omega$ [ $\text{s}^{-1}$ ]
0 BL	$23.5 \pm 42.8$	$37.6 \pm 24.5$	$52.5 \pm 23.4$	$0.3 \pm 0.02$
0.5 BL	$16.2 \pm 5.7$	$12.3 \pm 2.4$	$23.1 \pm 9.1$	$0.1 \pm 0.01$

The average position errors along  $x$ - and  $y$ -axis ( $e_x$  and  $e_y$ ), average error ( $e$ ), and angular velocities ( $\omega$ ) are measured from ten trials.

sprocketlike trajectory decreases, leading to lower positioning error and angular velocity of the orbiting microbeads. The simulation results also show that the amplitude of the sprocketlike trajectory increases with the tail length ratio [see Figs. 4(g) and 5(g)]. Therefore, the positioning error can be decreased by using lower tail length ratio within the range of  $1 < r < 2$ .

## V. CONCLUSION

Noncontact closed-loop control of nonmagnetic microbeads with average diameter of  $30 \mu\text{m}$  was achieved in 2-D space. This manipulation was controlled by the transmitted forces to the microbeads through flow-fields of rotating two-tailed soft microrobots under the influence of rotating magnetic fields. Our simulations and experimental results showed the ability to couple the microbeads to the rotating microrobot and allowed them to orbit along sprocketlike trajectories. The geometry of these trajectories depended on the tail length ratio of the microrobot, frequency of rotation, and the distance between the orbiting microbead and the microrobot. The angular velocity of the orbiting microbeads was characterized for rigid and flexible one- and two-tailed microrobots, and showed a decrease nearly as  $|\mathbf{p}|^{-2}$  with the distance to the center of rotation and with the tail length ratio. This characterization was used as a basis for a closed-loop control system that combined flagellar propulsion and rotations to achieve noncontact manipulation of the microbeads. Our closed-loop control system achieved an average position error of  $23.1 \pm 9.1 \mu\text{m}$  ( $n = 10$ ), and we demonstrated the ability of the microrobot to swim away from the vicinity of the positioned microbead without affecting the manipulation accuracy.

As part of future studies, the noncontact manipulation will be achieved using multiple two-tailed microrobots and our control strategy will be modified to control multiple microbeads based on the concept of virtual fluidic channel presented by Ye *et al.* [19]. The simultaneous noncontact manipulation using more than one microrobot will enable us to achieve noncontact microassembly in relatively sophisticated scenarios. We will also use the two-tailed microrobots to develop a reconfigurable microfluidic pump due to its ability to swim and create local flow-fields. The closed-loop control system will be implemented to achieve noncontact micromanipulation in 3-D space. The rotational flow-field created by the two-tailed microrobot can achieve fluidic trapping of microbeads located at different vertical distances. Therefore, our electromagnetic system has to be modified to localize the microrobot and the microbeads in 3-D space and our numerical model will be extended to predict the 3-D flow-fields in the workspace. In addition, our system

will be modified to manipulate and sort biological samples and cells. The noncontact manipulation strategy presented in this work decreased the risk of contamination that is likely to be encountered in this application.

## REFERENCES

- [1] S. Floyd, C. Pawashe, and M. Sitti, "Two-dimensional contact and non-contact micromanipulation in liquid using an untethered mobile magnetic microrobot," *IEEE Trans. Robot.*, vol. 25, no. 6, pp. 1332–1342, Dec. 2009.
- [2] K. E. Peyer, L. Zhang, and B. J. Nelson, "Localized non-contact manipulation using artificial bacterial flagella," *Appl. Phys. Lett.*, vol. 99, Sep. 2011, Art. no. 174101.
- [3] T. Petit, L. Zhang, K. E. Peyer, B. E. Kratochvil, and B. J. Nelson, "Selective trapping and manipulation of microscale objects using mobile microvortices," *Nano Lett.*, vol. 12, pp. 156–160, Nov. 2011.
- [4] E. Diller and M. Sitti, "Three-dimensional programmable assembly by untethered magnetic robotic micro-grippers," *Adv. Functional Mater.*, vol. 24, no. 28, pp. 4397–4404, Jul. 2014.
- [5] M. P. Kummer *et al.*, "OctoMag: An electromagnetic system for 5-DOF wireless micromanipulation," *IEEE Trans. Robot.*, vol. 26, no. 6, pp. 1006–1017, Dec. 2010.
- [6] F. Guo *et al.*, "Three-dimensional manipulation of single cells using surface acoustic waves," *Proc. Nat. Acad. Sci. USA*, vol. 113, no. 6, pp. 1522–1527, Jan. 2016.
- [7] S. Martel and M. Mohammadi, "Towards mass-scale micro-assembly systems using magnetotactic bacteria," *Int. Manuf. Sci. Eng. Conf.*, vol. 2, no. 6, pp. 487–492, Jun. 2011.
- [8] S. Martel, C. C. Tremblay, S. Ngakeng, and G. Langlois, "Controlled manipulation and actuation of micro-objects with magnetotactic bacteria," *Appl. Phys. Lett.*, vol. 89, no. 23, pp. 1–3, Nov. 2006.
- [9] S. Martel and M. Mohammadi, "Using a swarm of self-propelled natural microrobots in the form of flagellated bacteria to perform complex micro-assembly tasks," in *Proc. IEEE Int. Conf. Robot. Autom.*, May 2010, pp. 500–505.
- [10] B. K. Chen, Y. Zhang, and Y. Sun, "Active release of microobjects using a MEMS microgripper to overcome adhesion forces," *J. Microelectromech. Syst.*, vol. 18, no. 3, pp. 652–659, May 2009.
- [11] Z. Zhang, X. Wang, J. Liu, C. Dai, and Y. Sun, "Robotic micromanipulation: Fundamentals and applications," *Annu. Rev. Control, Robot., Auton. Syst.*, vol. 2, pp. 181–203, Dec. 2018, doi: [10.1146/annurev-control-053018-023755](https://doi.org/10.1146/annurev-control-053018-023755).
- [12] K. Kim, X. Liu, Y. Zhang, and Y. Sun, "Nanonewton force-controlled manipulation of biological cells using a monolithic MEMS microgripper with two-axis force feedback," *J. Micromech. Microeng.*, vol. 18, no. 5, Apr. 2008, Art. no. 055013.
- [13] J. Randhawa, T. Leong, N. Bassik, B. Benson, M. Jochmans, and D. Gracias, "Pick-and-place using chemically actuated microgrippers," *J. Amer. Chem. Soc.*, vol. 130, no. 51, pp. 17238–17239, Dec. 2008.
- [14] T. Leong, C. Randall, B. Benson, N. Bassik, G. Stern, and D. Gracias, "Tetherless thermobiochemically actuated microgrippers," *Proc. Nat. Acad. Sci.*, vol. 106, no. 3, pp. 703–708, Jan. 2009.
- [15] S. Fusco *et al.*, "Self-folding mobile microrobots for biomedical applications," in *Proc. IEEE Int. Conf. Robot. Autom.*, Sep. 2014, pp. 3777–3782.
- [16] J.-C. Kuo, H.-W. Huang, S.-W. Tung, and Y.-J. Yang, "A hydrogel-based intravascular microgripper manipulated using magnetic fields," *Sensors Actuator A, Physical*, vol. 211, pp. 121–130, May 2014.
- [17] J. Zhang, O. Onaizah, K. Middleton, L. You, and E. Diller, "Reliable grasping of three-dimensional untethered mobile magnetic microgripper for autonomous pick-and-place," *IEEE Robot. Autom. Lett.*, vol. 2, no. 2, pp. 835–840, Apr. 2017.

- [18] C. Pawashe, S. Floyd, E. Diller, and M. Sitti, "Two-dimensional autonomous microparticle manipulation strategies for magnetic microrobots in fluidic environments," *IEEE Trans. Robot.*, vol. 28, no. 2, pp. 467–477, Apr. 2012.
- [19] Z. Ye, E. Diller, and M. Sitti, "Micro-manipulation using rotational fluid flows induced by remote magnetic micro-manipulators," *J. Appl. Phys.*, vol. 112, no. 6, Aug. 2012, Art. no. 064912.
- [20] H.-W. Tung, K. E. Peyer, D. F. Sargent, and B. J. Nelson, "Noncontact manipulation using a transversely magnetized rolling robot," *Appl. Phys. Lett.*, vol. 103, no. 11, Aug. 2013, Art. no. 114101.
- [21] C. Hu, S. Pané, and B. J. Nelson, "Soft micro- and nanorobotics," *Annu. Rev. Control, Robot., Auton. Syst.*, vol. 1, pp. 53–75, May 2018.
- [22] R. Cortez, "The method of regularized Stokeslets," *SIAM J. Scientific Comput.*, vol. 23, no. 4, pp. 1204–1225, Jul. 2001.
- [23] J. J. Abbott, K. E. Peyer, L. Dong, and B. Nelson, "How Should Microrobots Swim?" *Int. J. Robot. Res.*, vol. 28, no. 11/12, pp. 1434–1447, Jul. 2009.
- [24] C. Brennen and H. Winet, "Fluid mechanics of propulsion by Cilia and Flagella," *Annu. Rev. Fluid Mech.*, vol. 9, pp. 339–398, Jan. 1977.
- [25] J. Gray and H. J. Hancock, "The propulsion of sea-urchin spermatozoa," *J. Exp. Biol.*, vol. 32, no. 4, pp. 802–814, Dec. 1955.
- [26] I. S. M. Khalil *et al.*, "Swimming back and forth using planar flagellar propulsion at low Reynolds numbers," *Adv. Sci.*, vol. 5, no. 2, Dec. 2017, Art. no. 1700461.
- [27] C. H. Wiggins and R. E. Goldstein, "Flexive and propulsive dynamics of elastica at low Reynolds number," *Physical Rev. Lett.*, vol. 80, no. 17, pp. 3879–3882, Apr. 1998.
- [28] I. S. M. Khalil, A. F. Tabak, A. Klingner, and M. Sitti, "Magnetic propulsion of robotic sperms at low-Reynolds number," *Appl. Phys. Lett.*, vol. 109, Jul. 2016, Art. no. 033701.
- [29] E. M. Purcell, "Life at low Reynolds number," *Amer. J. Phys.*, vol. 45, no. 1, pp. 3–11, Jun. 1977.
- [30] M. P. Kummer, J. J. Abbott, B. E. Kartochvil, R. Borer, A. Sengul, and B. J. Nelson, "OctoMag: An electromagnetic system for 5-DOF wireless micromanipulation," *IEEE Trans. Robot.*, vol. 26, no. 6, pp. 1006–1017, Dec. 2010.
- [31] I. S. M. Khalil *et al.*, "Independent actuation of two-tailed microrobots," *IEEE Robot. Autom. Lett.*, vol. 3, no. 3, pp. 1703–1710, Jul. 2018.



**Islam S. M. Khalil** (Member, IEEE) received the Ph.D. degree in mechatronics engineering from Sabanci University, Istanbul, Turkey, in 2011.

He became a Postdoctoral Research Associate with the Robotics and Mechatronics research group and MIRA Institute for Biomedical Technology and Technical Medicine, University of Twente, Enschede, The Netherlands. In 2014, he became an Assistant Professor with the Department of Mechatronics, German University in Cairo, New Cairo, Egypt, where he directed the Medical Micro and Nano Robotics

Laboratory. In 2018, he was appointed as an Associate Professor with the same department. In 2019, he became an Assistant Professor with the Department of Biomechanical Engineering, University of Twente. His research interests include modeling, design, and control of soft microrobots, biologically inspired systems, motion control systems, mechatronics system design, and untethered magnetic micro/nanorobotics with applications to micro/nanomanipulation, magnetic manipulation and targeted drug delivery.



**Anke Klingner** received the Ph.D. degree in applied physics in the field of electrowetting from Ulm University, Ulm, Germany, in 2004. She studied with the Technical University of Dresden, Dresden, Germany and one year with Duke University, Durham, NC, USA. She received the Diploma in Physics from the Technical University of Dresden.

She is currently affiliated with the Physics Department, German University in Cairo, New Cairo, Egypt. She is a Member of the Medical Micro and Nano robotics Laboratory, German University in Cairo. Her

research interests include physical modeling of microrobots, material characterization, fabrication of soft microrobots and biologically inspired systems.



**Youssef Hamed** received the bachelor's degree in mechatronics engineering from the German University in Cairo, New Cairo, Egypt, in 2018, where he is currently working toward M.S. degree with the Mechatronics Department and is investigating magnetic control of soft microrobots.



**Yehia S. Hassan** received the bachelor's degree in mechatronics engineering from the German University in Cairo, New Cairo, Egypt, in 2018.

He is currently a Production Management Engineer. His research interests include motion control, product design, and industrial automation.



**Sarthak Misra** (Member, IEEE) received the master's degree in mechanical engineering from McGill University, Montreal, QC, Canada, in 2001, and the doctoral degree in mechanical engineering from The Johns Hopkins University, Baltimore, MD, USA, in 2009.

He is currently a Full Professor with the Department of Biomechanical Engineering, University of Twente, Enschede, The Netherlands, and also affiliated with the Department of Biomedical Engineering, University of Groningen, Groningen, Netherlands,

and University Medical Center Groningen, Groningen, The Netherlands. Prior to commencing his doctoral studies, he was a Dynamics and Controls Analyst with the International Space Station Program. His research interests include surgical robotics and medical microrobotics.

Prof. Misra was the recipient of the European Research Council Starting, Proof-of-Concept, and Consolidator Grants and the Netherlands Organization for Scientific Research VENI and VIDI Awards. He is a Co-Chair of the Robotics and Automation Society Technical Committee on Surgical Robotics and a Co-Chair of the International Federation of Automatic Control Technical Committee on Biological and Medical Systems.